Citation: Zhaokun Ren, Yue Zhang, Yunxiang Wang, et al. Study on numerical simulation about motion trajectory of ice crystal particles under different injection conditions in wind tunnel. *Journal of Harbin Institute of Technology (New Series)*. DOI:10.11916/j.issn.1005-9113.25005

Study on Numerical Simulation about Motion Trajectory of Ice Crystal Particles under Different Injection Conditions in Wind Tunnel

*Zhaokun Ren**, *Yue Zhang*, *Yunxiang Wang*, *Zhanyuan Ma and Chen Bu*

(*AVIC Aerodynamic Research Institute*, *Harbin 150001*, *China*)

Abstract: Ice crystal icing is an important cause of accidents in aircraft engines. Ice formation in aircraft engines can cause internal blades to freeze, affecting the quality of the air flow field and blocking the flow path. On the other hand, the entry of ice crystal particles into the combustion chamber can cause a decrease in temperature or even flameout, leading to engine surge or even shutdown. Therefore, it is necessary to conduct multiphase flow tests on ice crystals for aircraft components such as aircraft engines. Conducting ice crystal multiphase flow tests on aircraft is a very effective research method, but it requires the construction of an ice crystal multiphase flow test platform that meets relevant technical requirements. The paper focuses on the relevant experimental requirements and combines wind tunnel test structures to conduct multiphase flow numerical simulations on various forms of jet pipelines, obtaining particle motion distribution results. After comparison, the optimal form of jet structure is obtained, providing the best selection scheme for the design of relevant wind tunnel structures.

Keywords: ice crystal; wind tunnel; numerical simulation; multiphase flow; jet pipelines

CLC number: V233.94 **Document code**: A **Article ID**: 1005-9113(2025)00-0000-18

0 Introduction

During high-altitude flight, aircraft may experience icing, including wing icing and engine icing. Researchers have found that wing icing and aircraft engine icing belong to two different mechanisms. Wing icing mainly occurs on the surface of the wing, and the altitude at which icing occurs is below 7000 m. The icing of aircraft engines mainly includes the short cabin lip, intake duct, rotating hood, fan blades, support plates, and other parts. Ice crystal icing mainly occurs in the intake duct and fan blades, which belong to the internal flow field. When the internal flow field freezes, it mainly occurs at an altitude of over 7000 m, with only small ice crystal particles and no supercooled droplets. Therefore, it can be concluded that the icing of the internal flow field of aircraft engines is caused by small ice crystals[1-5]. The distribution of ice crystal particles and supercooled droplets is shown in Fig. 1. As shown, under the action of convective airflow, smaller ice crystal particles exist in cloud layers at higher altitudes, whereas supercooled droplets exist at altitudes lower than ice crystal particles due to their larger size.

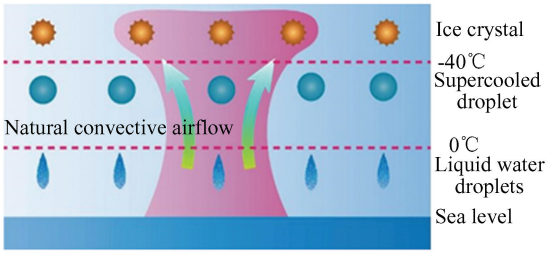

Fig.1 Schematic diagram of ice crystal particle distribution in nature

The schematic diagram in Fig.2 summarizes the areas where ice crystals freeze. As shown, the areas where ice crystals freeze are mainly concentrated in the entire stage of the low-pressure compressor and the first few stages of the high-pressure compressor blades. Owning to the internal temperature of aircraft engines being generally between 10 - 20℃, the ice crystal particles will partially melt at this temperature,

Received 2025-02-13.

* Corresponding author. Zhaokun Ren, Ph.D, Engineer. Email: dakun2008@163.com.

forming a liquid film on the surface. When they collide with the blades, they will bond and form an ice layer on the surface of the blades. The melting process of ice crystals is illustrated in Fig. 3. As shown, under the action of airflow, ice crystal particles enter the engine interior, causing partial melting of the non-spherical ice crystal surface and gradually transforming from a non-spherical shape to a spherical shape. On the other hand, smaller ice crystal particles will completely melt during their movement, whereas larger ice crystal particles will not completely melt. Ice crystal particles with a liquid film on their surface form a bond when they are contacting with engine blades, ultimately forming a liquid water film that continuously captures the subsequently impacted ice crystal particles, to form an ice layer.

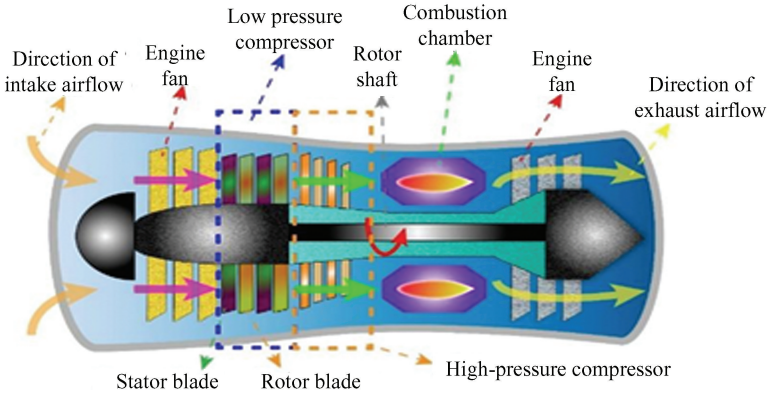

Fig.2 Schematic diagram of icing area in aircraft engine

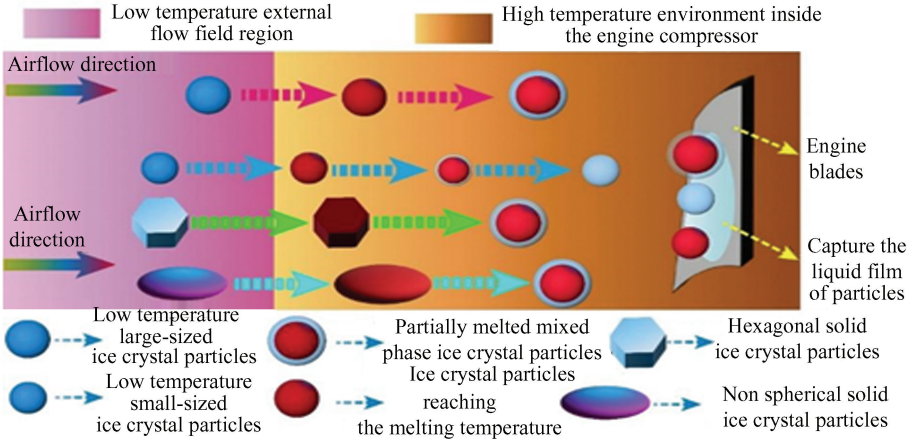

Fig.3 Schematic diagram of ice crystal melting process

The experimental research on ice crystal formation in aircraft engines requires the establishment of relevant testing platforms. Foreign countries have rich experience in aircraft engine icing test platforms, including the IRT (Iceing Research Tunnel) icing wind tunnel in the United States[6-7], the Arnold Engineering Development Center (AEDC) icing wind tunnel[8-9], the Modan Center icing wind tunnel in France[10-11], and the IWT (Icing Wind Tunnel) icing wind tunnel in Italy[12-14], all of which have conducted relevant experimental research on aircraft engine icing tests.

There are three main ways in which ice crystals are produced:

1) Utilize cloud chamber technology to generate ice crystals;

2) Use spray cooling to form ice crystals;

3) Form small-sized ice crystals by cutting and grinding larger ice cubes.

In many ice crystal icing wind tunnels, the

Propulsion System Lab (PSL) of NASA is a very typical representative[15]. The way to generate ice crystals is to use the droplets generated by the spray rake to form small ice crystal particles under the action of cold air. The ice crystal particles constantly hit the engine test model through the pipe, thus forming icing phenomenon. Cox & Company in the United States has built the Cox icing wind tunnel to simulate icing tests in ice crystal and mixed phase icing environments, using ice crystal particles generated by grinding[16].

The National Research Council of Canada (NRC) has also established ice crystal testing equipment[17]. The experimental equipment uses sheet ice prepared from deionized water, and the sheet ice is added to an ice mill to prepare ice crystal particles. While using a pipe to spray the ice crystal particles, another pipe sprays hot air to control the total temperature and humidity of the environment, forming a melting environment for the ice crystal particles[18].

In the process of experimental and simulation research on ice crystal particle spraying at home and abroad, there is not a relatively comprehensive study on the distribution of ice crystal particles. If the concentration distribution of ice crystal particles cannot meet the experimental requirements, it will affect the development of future ice crystal freezing test technology. In this article, multiphase flow numerical simulations were conducted for different spray structures of ice crystal pipelines, in order to determine the optimal structure among various constraints and provide suggestions and references for the design and testing of ice crystal spray test platforms in the future.

1 Numerical Simulation Model of Discrete Phase Multiphase Flow

The main method used for numerical simulation of multiphase flow of ice crystal particles is the Euler-Lagrange method, which uses the air field as the continuous phase and the Euler method for calculation, and the ice crystal particles as the discrete phase and the Lagrange method for calculation. Due to the small size of ice crystal particles and their volume fraction ranging from 10^{-5} to 10^{-6} in two-phase flow calculations, a unidirectional coupling method can be used for calculation, where the air field is calculated separately and the motion of ice crystal particles does not affect the air flow field[19-21].

When conducting multiphase flow simulation work, relevant conditional assumptions need to be made as follows:

1) Ice crystal particles will not break during their movement;

2) Ice crystal particles will not aggregate or collide during their movement;

3) Other physical parameters of ice crystal particles are constants;

4) It is assumed that ice crystal particles do not rotate during their movement;

5) The air temperature and ice crystal particle temperature are both set to −20℃;

Based on the above assumptions, the motion equation of ice crystal particles is established using Newton's second law: The forces exerted on ice crystal particles mainly include viscous resistance, gravity, buoyancy, pressure gradient force, Barcat force, Safman force, Magnus force, etc. Among them, viscous resistance is the main force that affects the trajectory of ice crystal particles. When the size of ice crystal particles is large, the influence of gravity must be considered, while other forces can be ignored due to their smaller impact[22].

$$m_i \frac{\mathrm{d}\vec{\boldsymbol{u}}_i}{\mathrm{d}t} = \vec{\boldsymbol{F}} \tag{1}$$

where, m_i is the mass of ice crystal particles; $\mathrm{d}\vec{\boldsymbol{u}}_i/\mathrm{d}t$ is the acceleration of ice crystal particle motion; $\vec{\boldsymbol{F}}$ is the force exerted on ice crystal particles.

$$\vec{\boldsymbol{F}} = \vec{\boldsymbol{D}} + m_i g \tag{2}$$

where, $\vec{\boldsymbol{D}}$ is the viscous resistance experienced by ice crystal particles during their motion; $m_i g$ is the gravity exerted on ice crystal particles; When the size of ice crystal particles is small, the influence of gravity can be ignored in Eq. (2)[23].

$$\vec{\boldsymbol{D}} = \frac{1}{2}\rho_{\mathrm{a}} C_{\mathrm{D}} |\vec{\boldsymbol{u}}_{\mathrm{a}} - \vec{\boldsymbol{u}}_i| \cdot (\vec{\boldsymbol{u}}_{\mathrm{a}} - \vec{\boldsymbol{u}}_{\mathrm{i}}) (\frac{1}{4}\pi d_{\mathrm{i}}^2) \tag{3}$$

where, C_{D} represents the drag coefficient; ρ_{a} is air density; d_{i} is the diameter of ice crystal particles; $\vec{\boldsymbol{u}}_{\mathrm{a}} = (u, v, w)$ is air velocity; $\vec{\boldsymbol{u}}_{\mathrm{i}}$ is the velocity of ice crystal particles;

The expression for the relative Reynolds number is as follows:

$$\mathrm{Re}_{\mathrm{rel}} = \frac{\rho_{\mathrm{a}} |u_{\mathrm{a}} - u_{\mathrm{i}}| d_{\mathrm{i}}}{\mu_{\mathrm{a}}} \tag{4}$$

where μ_a is the dynamic viscosity coefficient of air.

By substituting Eqs. (3) and (4) into Eq (1), the following equation can be obtained[24]:

$$\frac{\mathrm{d}\vec{\boldsymbol{u}}_{\mathrm{i}}}{\mathrm{d}t}=\frac{C_{\mathrm{D}}\mathrm{Re}_{\mathrm{rel}}}{24}\cdot\frac{18\mu_{\mathrm{a}}}{\rho_{\mathrm{i}}d_{\mathrm{i}}^{2}}(\vec{\boldsymbol{u}}_{\mathrm{a}}-\vec{\boldsymbol{u}}_{\mathrm{d}}) \tag{5}$$

In the paper, it is assumed that the shape of ice crystal particles is spherical, therefore a spherical resistance coefficient is applied, which is expressed as follows:

1) When $\mathrm{Re}_{\mathrm{rel}}<0.1$, $C_{\mathrm{D}}=\dfrac{24}{\mathrm{Re}_{\mathrm{rel}}}$;

2) When $0.1<\mathrm{Re}_{\mathrm{rel}}<1$, $C_{\mathrm{D}}=\dfrac{24}{\mathrm{Re}_{\mathrm{rel}}}(1+\dfrac{3\mathrm{Re}_{\mathrm{rel}}}{16})$;

3) When $1<\mathrm{Re}_{\mathrm{rel}}<1000$, $C_D=\dfrac{24}{\mathrm{Re}_{\mathrm{rel}}}(1+\dfrac{\mathrm{Re}_{\mathrm{rel}}^{(2/3)}}{6})$;

4) When $\mathrm{Re}_{\mathrm{rel}}>1000$, $C_{\mathrm{D}}=0.44$.

By combining other relevant equations, the motion trajectory of ice crystal particles can be obtained by Eq. (5).

For the calculation of the airflow field, the N-S (Navier-Stokes) equation considering viscosity is applied.

The continuity equation is as follows:

$$\frac{\partial\rho}{\partial t}+\nabla\cdot(\rho\vec{\boldsymbol{u}}_{\mathrm{a}})=0 \tag{6}$$

where ρ is air density ($\mathrm{kg\cdot m^{-3}}$); $\vec{\boldsymbol{u}}_{\mathrm{a}}$ is the velocity vector of air microelements ($\mathrm{m\cdot s^{-1}}$);

The momentum equation is as follows:

$$\frac{\partial(\rho_{\mathrm{a}}u)}{\partial t}+\nabla\cdot(\rho_{\mathrm{a}}u\vec{\boldsymbol{u}}_{\mathrm{a}})=-\frac{\partial p}{\partial x}+\frac{\partial\tau_{xx}}{\partial x}+\frac{\partial\tau_{yx}}{\partial y}+\frac{\partial\tau_{zx}}{\partial z}+\rho_{\mathrm{a}}F_x \tag{7}$$

$$\frac{\partial(\rho_{\mathrm{a}}v)}{\partial t}+\nabla\cdot(\rho_{\mathrm{a}}v\vec{\boldsymbol{u}}_{\mathrm{a}})=-\frac{\partial p}{\partial y}+\frac{\partial\tau_{xy}}{\partial x}+\frac{\partial\tau_{yy}}{\partial y}+\frac{\partial\tau_{zy}}{\partial z}+\rho_{\mathrm{a}}F_y \tag{8}$$

$$\frac{\partial(\rho_{\mathrm{a}}w)}{\partial t}+\nabla\cdot(\rho_{\mathrm{a}}w\vec{\boldsymbol{u}}_{\mathrm{a}})=-\frac{\partial p}{\partial z}+\frac{\partial\tau_{xz}}{\partial x}+\frac{\partial\tau_{yz}}{\partial y}+\frac{\partial\tau_{zz}}{\partial z}+\rho_{\mathrm{a}}F_z \tag{9}$$

where, p is the pressure on the air unit (Pa); F_x, F_y and F_z are the volumetric force on air microelements; τ_{xx}, τ_{yx}, τ_{zx}, τ_{xy}, τ_{yy}, τ_{zy}, τ_{xz}, τ_{yz} and τ_{zz} are the viscous stress component on the surface of the air element (Pa); $\vec{\boldsymbol{u}}_{\mathrm{a}}=(u,v,w)$ is air velocity;

The energy equation is as follows:

$$\frac{\partial}{\partial t}[\rho_{\mathrm{a}}(e+\frac{u_{\mathrm{a}}^2}{2})]+\nabla\cdot[\rho_{\mathrm{a}}(e+\frac{u_{\mathrm{a}}^2}{2})\vec{\boldsymbol{V}}]=\rho_{\mathrm{a}}\dot{q}+\frac{\partial}{\partial x}(k\frac{\partial T}{\partial x})+\frac{\partial}{\partial y}(k\frac{\partial T}{\partial y})+\frac{\partial}{\partial z}(k\frac{\partial T}{\partial z})-\frac{\partial(up)}{\partial x}-\frac{\partial(vp)}{\partial y}-\frac{\partial(wp)}{\partial z}+\frac{\partial(u\tau_{xx})}{\partial x}+\frac{\partial(u\tau_{yx})}{\partial y}+\frac{\partial(u\tau_{zx})}{\partial z}+\frac{\partial(v\tau_{xy})}{\partial x}+\frac{\partial(v\tau_{yy})}{\partial y}+\frac{\partial(v\tau_{zy})}{\partial z}+\frac{\partial(w\tau_{xz})}{\partial x}+\frac{\partial(w\tau_{yz})}{\partial y}+\frac{\partial(w\tau_{zz})}{\partial z}+\rho_{\mathrm{a}}\vec{\boldsymbol{F}}\cdot u_{\mathrm{a}}^2 \tag{10}$$

where $u_{\mathrm{a}}^2=u^2+v^2+w^2$, which represents the sum of squared velocities in all directions; e is the internal energy of air microelements ($e=c_{\mathrm{v}}T$); k is the thermal conductivity of air; c_{v} is the specific heat capacity of air at a constant volume ($\mathrm{J\cdot kg^{-1}\cdot K^{-1}}$); $\dot{q}$ is internal heat source ($\mathrm{J\cdot kg^{-1}}$); $\vec{\boldsymbol{F}}$ is body force.

The standard k-ε turbulence model is applied in the paper, which is widely used in flow field calculations in engineering. Because the multiphase flow numerical simulation structure in the paper is relatively complex and has a large number of grids. If other turbulence models are used, their convergence results are not optimistic. The equation is as follows:

$$\frac{\partial(\rho_{\mathrm{a}}k)}{\partial t}+\frac{\partial(\rho_{\mathrm{a}}ku_i)}{\partial x_i}=\frac{\partial}{\partial x_j}[(\mu+\frac{\mu_{\mathrm{t}}}{\sigma_{\mathrm{k}}})\frac{\partial k}{\partial x_j}]+G_{\mathrm{k}}+G_{\mathrm{b}}-\rho_{\mathrm{a}}\varepsilon-Y_{\mathrm{M}} \tag{11}$$

$$\frac{\partial(\rho_{\mathrm{a}}\varepsilon)}{\partial t}+\frac{\partial(\rho_{\mathrm{a}}\varepsilon u_i)}{\partial x_i}=\frac{\partial}{\partial x_j}[(\mu+\frac{\mu_{\mathrm{t}}}{\sigma_{\mathrm{k}}})\frac{\partial\varepsilon}{\partial x_j}]+C_{1\varepsilon}\frac{\varepsilon}{k}(G_{\mathrm{k}}+C_{3\varepsilon}G_{\mathrm{b}})-C_{2\varepsilon}\rho_{\mathrm{a}}\frac{\varepsilon^2}{k} \tag{12}$$

where, G_{k} and G_{b} are the turbulence energy generation terms; Y_{M} is dissipation term; $C_{1\varepsilon}$, $C_{2\varepsilon}$ and $C_{3\varepsilon}$ are constants in the model; σ_{k} and σ_{ε} are the turbulent Prandtl numbers for turbulent kinetic energy and dissipation rate, respectively.

The calculated turbulent viscosity coefficient is as follows:

$$\mu_{\mathrm{t}}=\rho_{\mathrm{a}}C_{\mu}\frac{k^2}{\varepsilon} \tag{13}$$

$$C_{\mu}=0.09 \tag{14}$$

In the paper, firstly, a stable flow field distribution is obtained by calculating the air flow field, and then a discrete multiphase flow model is initiated. Therefore, the study adopts one-way coupling, which only considers the influence of the air flow field to ice crystal particles and ignores the

influence of ice crystal particles to the flow field.

2 Design Scheme for Ice Crystal Particle Jet Pipeline

In Fig.4, a schematic diagram of the ice crystal jet test wind tunnel is shown, which only shows a part of the stable section, and the structure and size of the test section. The stable section is a circular shape with a diameter of 5000 mm, and the size of the test section is 3350 mm×1700 mm×600 mm. The wind tunnel adopts a double contraction section design.

In Fig.5, a schematic diagram of a single tube jet structure is shown, with a pipeline size of DN80 and a length of 6451 mm. This size is chosen because the wind tunnel requires vacuum treatment during operation to create a low-pressure environment at an altitude of 14000 m. The high-pressure air is transported by the pipeline when spraying ice crystal particles, so the spraying pipeline is constantly spraying air. If the pipeline size is too large, the excessive air flow rate sprayed by the spraying pipeline will cause the vacuum environment to be unable to meet the requirements.

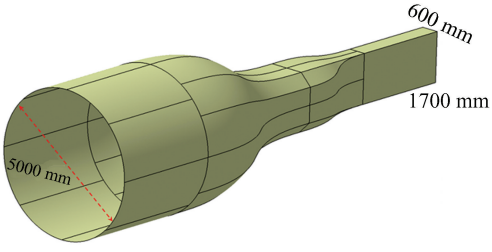

Fig. 4 Schematic diagram of ice crystal particle jet test wind tunnel

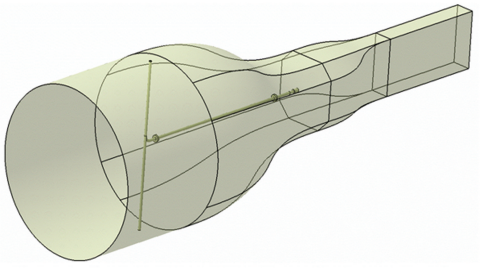

Fig.5 Schematic diagram of DN80 single tube installation structure

In Fig.6, a three-pipe structure with a size of DN50 is shown. The vertical spacing between the three pipes is 600 mm, the horizontal spacing is 120 mm, and the pipe length is 6451 mm. In Fig.7, a schematic diagram of the position distribution of the three-pipeline structure is shown. A DN50 sized pipeline is used here, due to depending on the actual situation, if the pipeline size is too large, it will cause the nozzle to spray an excessive amount of air flow, resulting in the inability to achieve the required low-pressure environment for use.

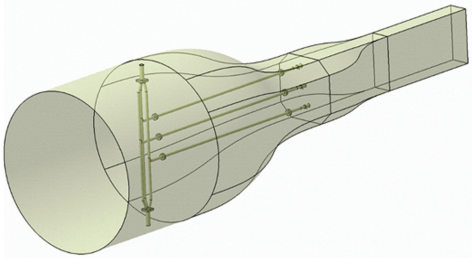

Fig.6 Schematic diagram of three-pipe spray structure with horizontal spacing of 120 mm and vertical spacing of 600 mm

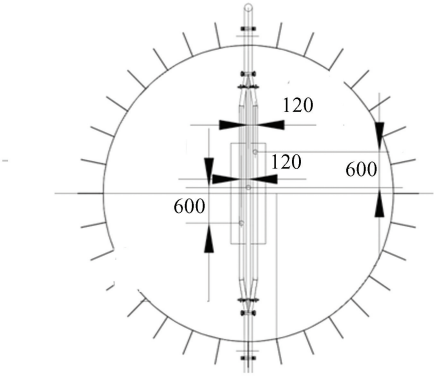

Fig.7 Schematic diagram of the distribution of three-tube spray nozzles with a horizontal spacing of 120 mm and a vertical spacing of 600 mm

In Figs.8 and 9, the schematic diagram shows a three-pipe spray structure with a vertical spacing of 300 mm, a pipeline length of 6451 mm, a size of DN50, and distributed in the same plane. Compared with Figs.6 and 7, the modified jet structure has changed the originally slanted distribution of the three pipes to a uniform distribution on the same plane, and the spacing between the pipes has been changed from 600 mm to 300 mm to observe the distribution changes of ice crystal particles.

In Fig.10, the length of the pipeline in Fig.8 has been modified from 6451 mm to 3225 mm to observe the effect of pipeline length on the concentration distribution of ice crystal particles. Other dimensions and distribution have not changed.

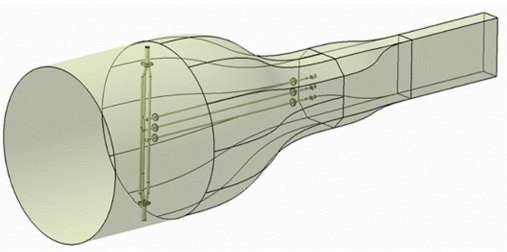

Fig.8 Schematic diagram of a three-pipe spray structure distributed in the same plane with a vertical spacing of 300 mm

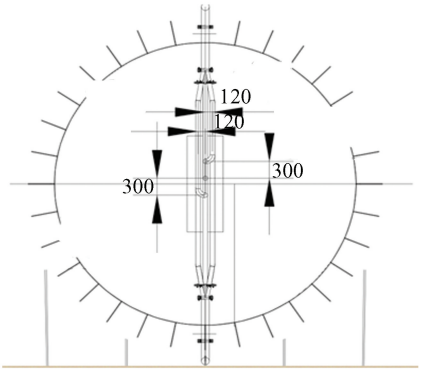

Fig.9 Schematic diagram of the distribution of three nozzle structures with vertical spacing of 300 mm distributed in the same plane

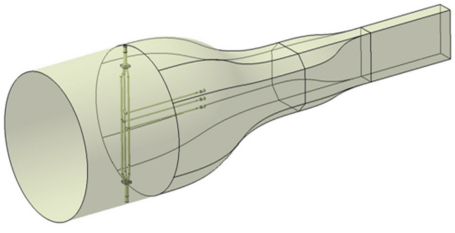

Fig.10 Schematic diagram of the distribution of three pipe spray structure nozzles with a pipeline length of 3225 mm, distributed in the same plane and vertically spaced at 300 mm intervals

In Fig. 11, a schematic diagram of the distribution of spray pipes is shown after the pipe length is shortened to 200 mm. Compared with the pipe shown in Fig.10, the spray pipe length is very short, in order to observe the effect of the spray pipe length on the distribution of ice crystal concentration. In Fig.12, a schematic diagram of the structure of the spray nozzle is shown, which mainly includes two airflow channels, namely the airflow inlet and outlet, and the inlet and outlet of the air supply system. The airflow inlet and outlet are mainly applied for the transportation and spraying of ice crystal particles, while the air supply system is mainly applied to use high-pressure air to disperse ice crystal particles and prevent agglomeration.

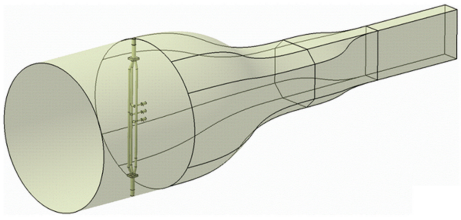

Fig.11 Schematic diagram of the distribution of three nozzle structures with a pipeline length of 200 mm, distributed in the same plane and vertically spaced at 300 mm intervals

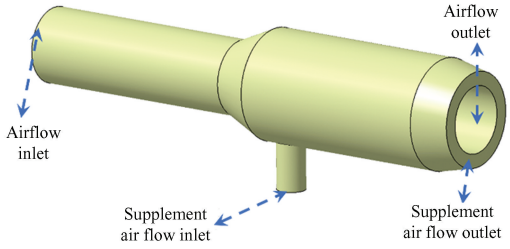

Fig.12 Schematic diagram of spray nozzle structure

3 Analysis on Numerical Simulation Results of Multiphase Flow about Ice Crystal Particles

In practical situations, it is necessary to determine the optimal ice crystal spraying structure and position through numerical simulation. Therefore, in the paper, several structures listed in Section 3 are numerically simulated to observe the flow field quality and the distribution and motion of ice crystal particles, providing reference for the construction of subsequent ice crystal spraying test wind tunnels.

The nozzle air supply system and nozzle inlet are set with pressure inlet conditions (gauge pressure of 0.09 MPa), with ice crystal particle flow rates set at 0.1 kg/s, 0.5 kg/s. In the actual experimental process, the desired concentration of ice crystal particles in the test section is between 1 g/m^3 and 5 g/m^3, and the test wind speed is 100 m/s. After calculation, the wind speed at the stable section entrance is 5.195 m/s. When the wind speed in the experimental section is 100 m/s and the given ice crystal particle flow rate is 0.1 kg/s, the corresponding particle concentration in the experimental section is 1 g/m^3. When the ice crystal particle flow rate is 0.5 kg/s, the corresponding particle

concentration in the experimental section is 5 g/m^3.

The natural density of ice crystal particles in the paper is 920 kg/m^3, and the size of ice crystal particles varies continuously during the actual experimental process. Here, the particle sizes are set to 20, 30, 40, 50, 60, 70, 80, 90, 100, 110, 120, 130, and 140 μm, respectively. The average ice crystal particle size used for calculation is 85 μm.

When considering the impact of jet ducts on airflow quality, refers to GJB 1179A - 2012, 《Requirements for Flow Quality of Low and High Speed Wind Tunnels》. And the influence of different pipeline injection structures on the airflow deflection angle was calculated. In this paper, 75% of the size on the middle section in the experimental section was selected as the reference area.

The velocity cloud maps and ice crystal particle concentration cloud maps of DN80 single tube under different injection conditions are shown in Figs. 13 - 16. Here DPM represents the discrete phase model. Due to the jet pipeline spraying ice crystal particles to transport airflow, and the high jet velocity of this airflow, a very obvious jet zone is formed, and the velocity in this jet zone is higher than that in other areas of the experimental section. From the cloud map of ice crystal particle concentration distribution, it can be observed that ice crystal particles are mainly concentrated in the middle of the experimental section and will not be evenly distributed throughout the entire experimental section. On the entire cross-section, it can be observed that at the nozzle outlet position, ice crystal particles firstly exhibit diffusion phenomenon, and then as they continue to move, the particle trajectory shrinks and forms a jet state in the experimental section area. Due to the small size of ice crystal particles, which are mainly subjected to the drag force of air, while other forces, such as gravity, pressure gradient force, Basset force, saffman force, Magnus force, are ignored due to their small size. Therefore, the motion trajectory of ice crystal particles can also be approximated as the motion trajectory of air flow. From the figures of particle contentration cloud map shown in Figs. 13 (b) - 28 (b), it can also be observed that the ice crystal particles did not settle due to the high airflow velocity and small size of the ice crystal particles, thus no settling phenomenon occurred. Comparing different ice crystal particle concentrations, it can be found that the ice crystal particle concentration is mainly concentrated in the middle of the experimental section, and the coverage area is basically the same.

When ice crystal particles are ejected from the nozzle and move to the middle position of the test section, their concentration area should appear circular. However, it can be seen that it is not a conventional circle, which may be related to the quality of the grid division. However, the number of grids already in this paper is generally over 20 million. If the number of grids continues to increase, it will exceed the computational capacity.

In Figs.17-20, the three-tube jet structure with a horizontal spacing of 120 mm and a vertical spacing of 600 mm is shown, along with the distribution of ice crystal concentration and the distribution of air velocity cloud maps under different ice crystal particle flow rates. From the figures, the motion trajectory of ice crystal particles presents a three-jet state. From the cross-section in the middle section of the experimental section, the concentration of ice crystal particles still corresponds to the original jet position. After being ejected from the nozzle, ice crystal particles also exhibit a trend of diffusion followed by contraction.

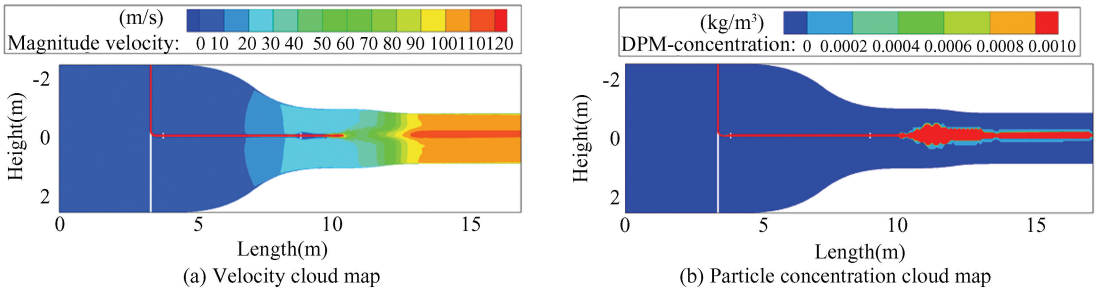

(a) Velocity cloud map (b) Particle concentration cloud map

Fig.13 Velocity cloud map and particle concentration cloud map at a wind speed of 100 m/s in the 1 g/m^3 particle concentration test section under a single tube state

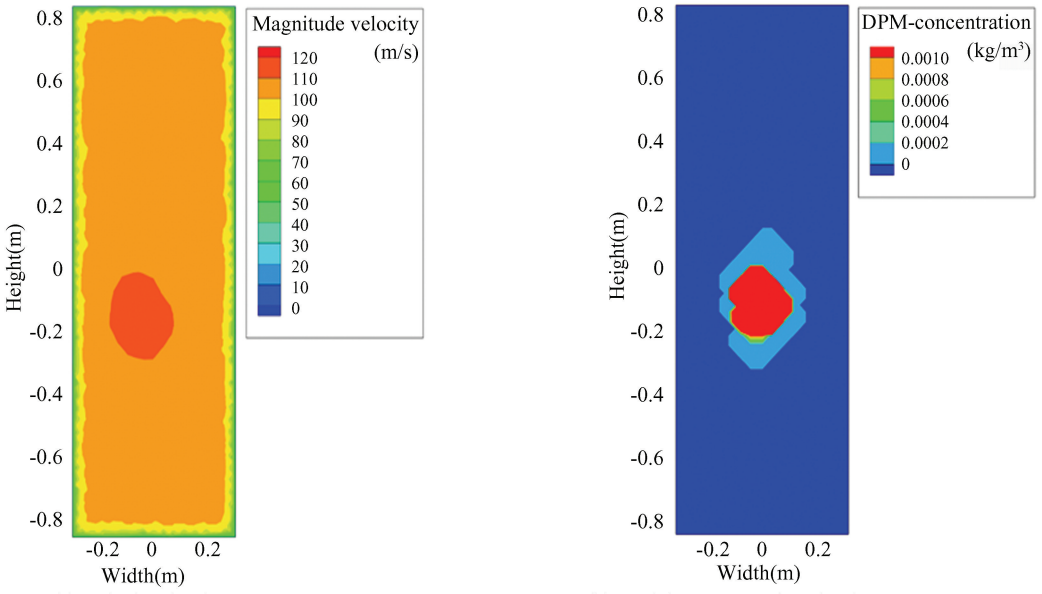

(a) Velocity cloud map (b) Particle concentration cloud map

Fig.14 Velocity cloud map and particle concentration cloud map at the middle section of the test section with a wind speed of 100 m/s and a particle concentration of 1 g/m³ in a single tube state

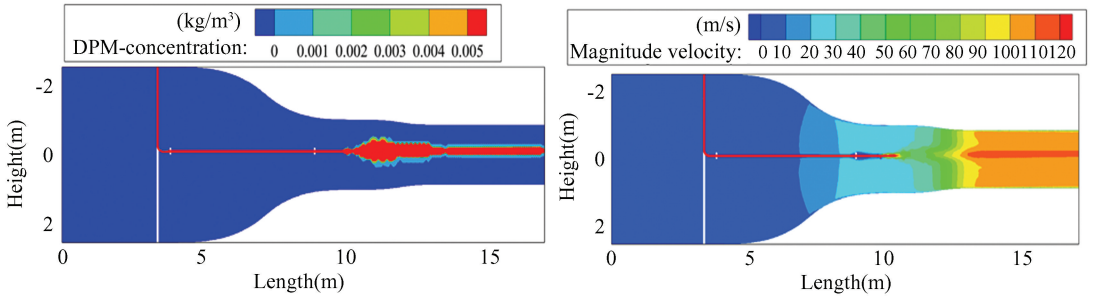

(a) Velocity cloud map (b) Particle concentration cloud map

Fig.15 Velocity cloud map and particle concentration cloud map of the 5 g/m³ particle concentration test section in a single tube state at a wind speed of 100 m/s

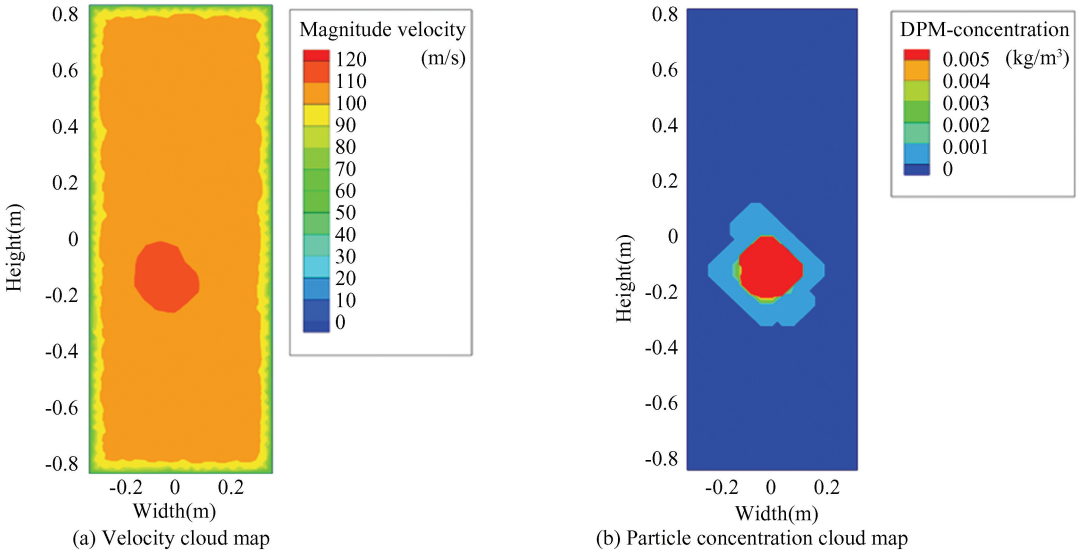

(a) Velocity cloud map (b) Particle concentration cloud map

Fig.16 Velocity cloud map and particle concentration cloud map at the middle section of the test section with a wind speed of 100 m/s and a particle concentration of 5 g/m³ in a single tube state

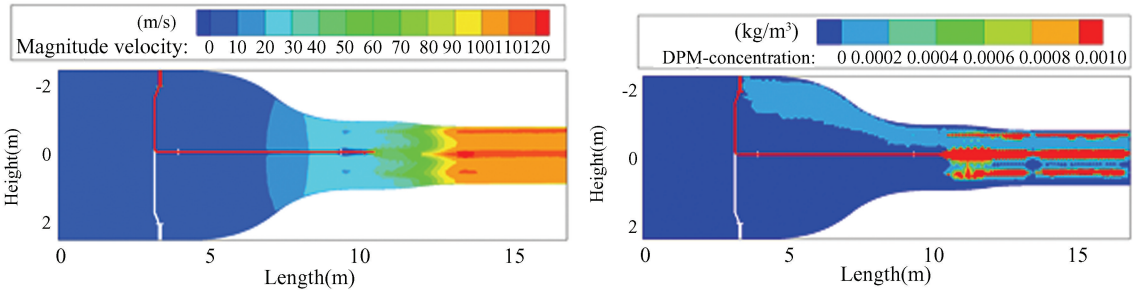

(a) Velocity cloud map (b) Particle concentration cloud map

Fig.17 Three tube spray structure with horizontal spacing of 120 mm and vertical spacing of 600 mm, velocity cloud map and particle concentration cloud map of 1 g/m³ particle concentration test section at a wind speed of 100 m/s

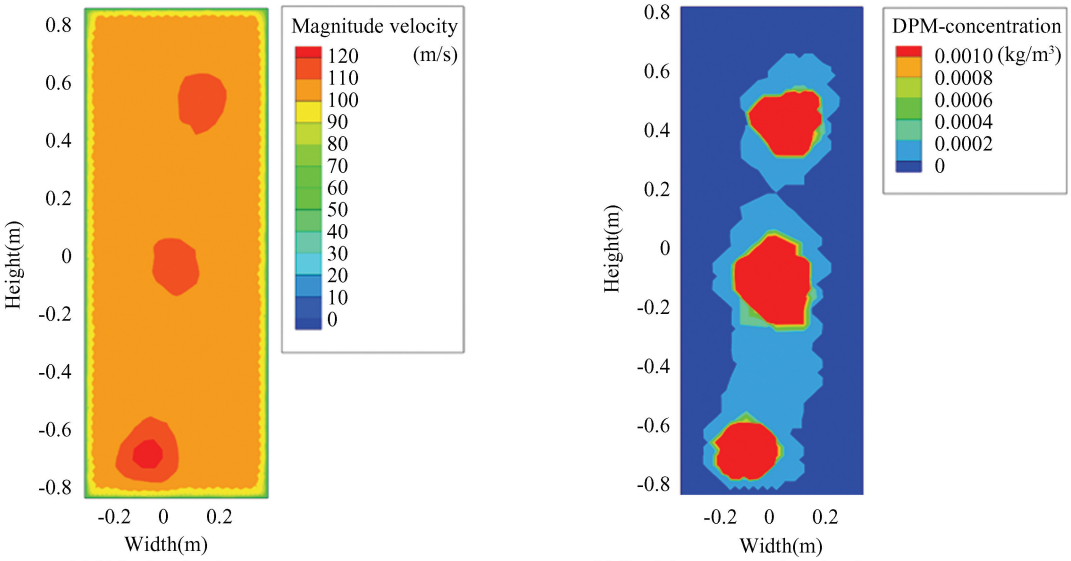

(a) Velocity cloud map (b) Particle concentration cloud map

Fig.18 Three tube spray structure with horizontal spacing of 120 mm and vertical spacing of 600 mm, velocity cloud map and particle concentration cloud map of 1 g/m³ particle concentration at the middle of test section at a wind speed of 100 m/s

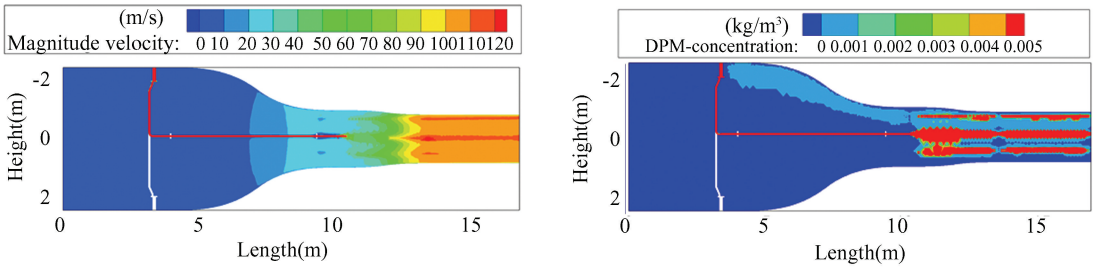

(a) Velocity cloud map (b) Particle concentration cloud map

Fig.19 Three tube spray structure with horizontal spacing of 120 mm and vertical spacing of 600 mm, velocity cloud map and particle concentration cloud map of 5 g/m³ particle concentration test section at a wind speed of 100 m/s

In Figs. 21 – 24, numerical simulation results of ice crystal spraying were analyzed for a three-tube spraying structure with a pipeline length of 6451 mm and a vertical spacing of 300 mm, distributed in the same plane. From the figures, after adjusting the pipes to be distributed in the same plane, the ice crystal particles sprayed from each pipe can now continuously gather in the middle position of the experimental section. On the other hand, the ice crystal particles ejected from the nozzle exhibit a diffusion trend, resulting in a more significant increase in the zone of fused ice crystal particles.

Meanwhile, due to the influence of airflow contraction before entering the experimental section, there was a certain degree of particle separation between the contraction section and the experimental section. However, this phenomenon disappeared in the experimental section.

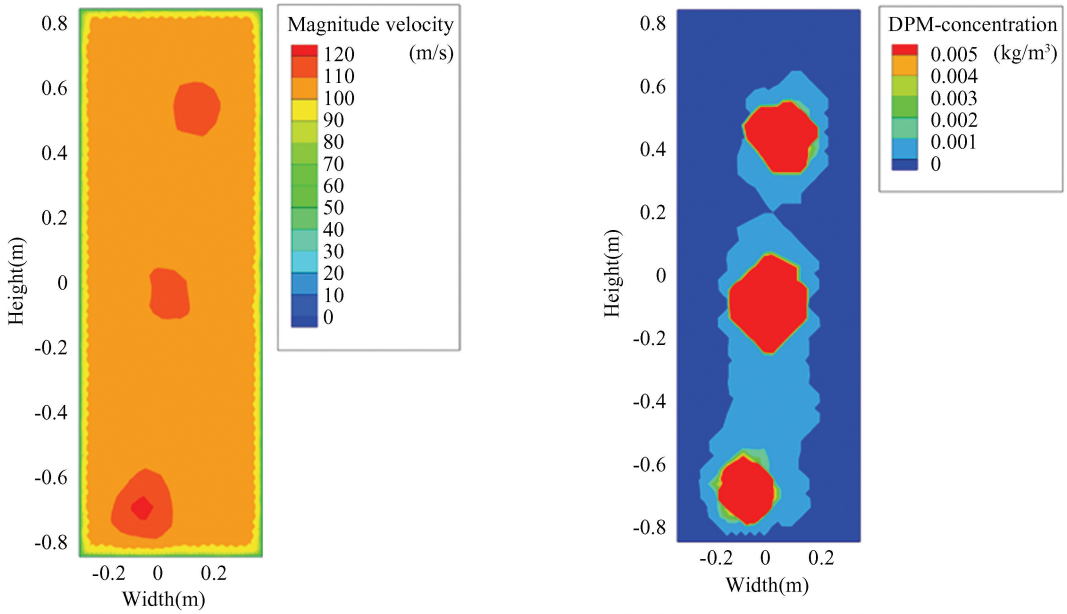

(a) Velocity cloud map (b) Particle concentration cloud map

Fig.20 Three tube spray structure with horizontal spacing of 120 mm and vertical spacing of 600 mm, velocity cloud map and particle concentration cloud map of 5 g/m³ particle concentration at the middle of test section at a wind speed of 100 m/s

In Figs. 25 – 28, numerical simulation results of ice crystal spraying were analyzed for three-pipe spraying structures with pipe lengths of 3225 mm and 200 mm and vertical spacing of 300 mm, distributed in the same plane. Compared with the pipeline length of 6451 mm, it can be seen from the results that the ice crystal aggregation area is still in the middle position of the experimental section, but the area is slightly smaller. When the pipeline length is 200 mm, the diffusion area of ice crystal particles is the largest at the outlet of the nozzle, because the nozzle is located in the stable section, with lower air velocity and a certain distance from the contraction section, making it easier for ice crystal particles to diffuse. As the ice crystal particles move, the airflow velocity gradually increases and continuously contracts, resulting in the phenomenon of ice crystal particles contracting into a jet. In summary, compared with long pipelines, the ice crystal distribution in the cross-section of the test section is more continuous, and the test effect will be better.

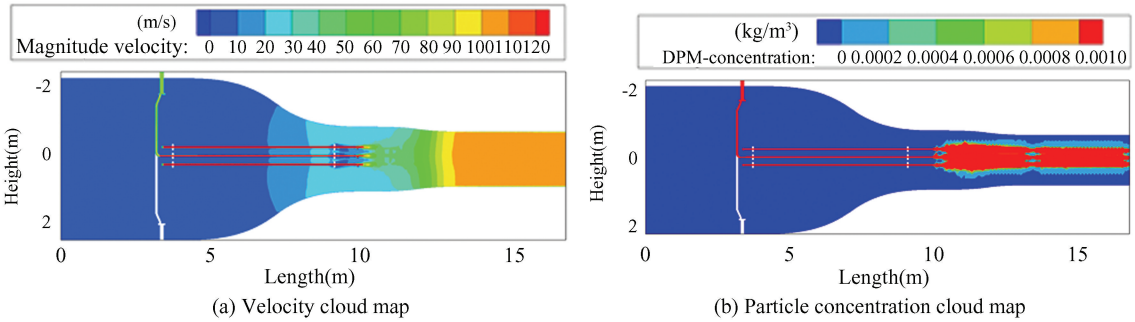

(a) Velocity cloud map (b) Particle concentration cloud map

Fig.21 Three pipe spray structure distributed in the same plane with a vertical spacing of 300 mm, pipe length of 6451 mm, 1 g/m³ particle concentration test section velocity cloud map and particle concentration cloud map at a wind speed of 100 m/s

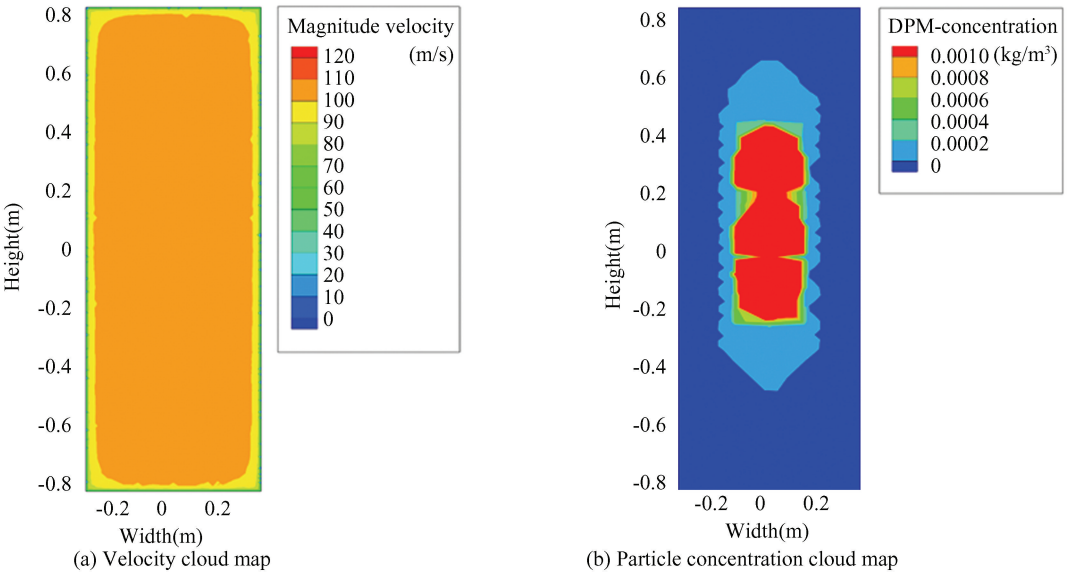

(a) Velocity cloud map (b) Particle concentration cloud map

Fig.22 Three pipe spray structure distributed in the same plane with a vertical spacing of 300 mm, pipe length of 6451 mm, 1 g/m³ particle concentration test section velocity cloud map and particle concentration cloud map at the middle section of the test section under a wind speed of 100 m/s

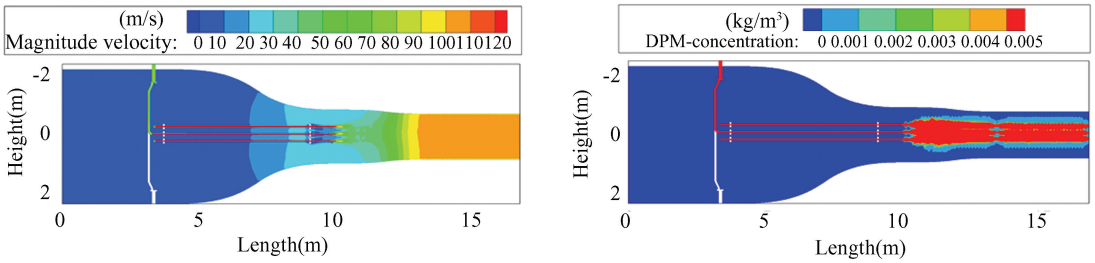

(a) Velocity cloud map (b) Particle concentration cloud map

Fig.23 Three pipe spray structure distributed in the same plane with a vertical spacing of 300 mm, pipe length of 6451 mm, 5 g/m³ particle concentration test section velocity cloud map and particle concentration cloud map at a wind speed of 100 m/s

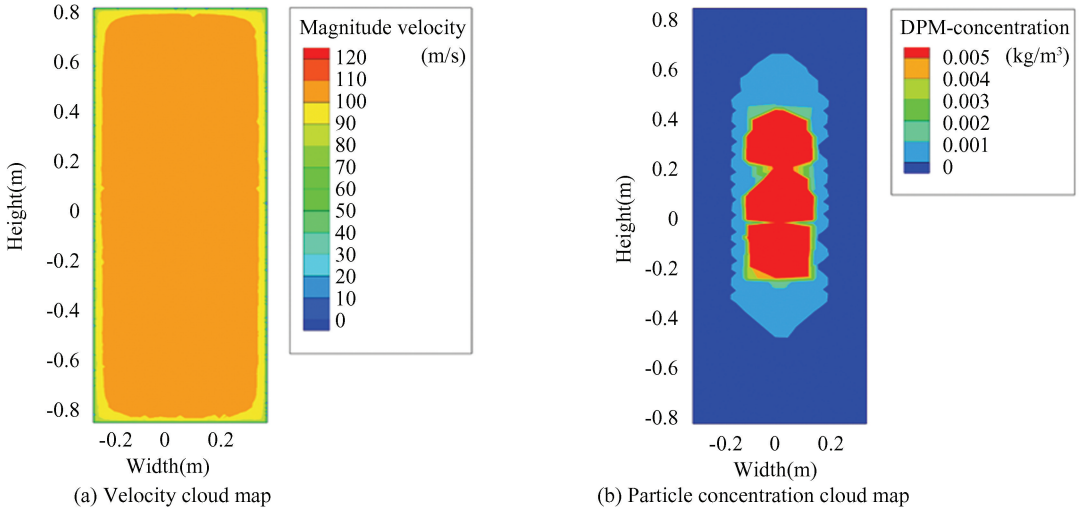

(a) Velocity cloud map (b) Particle concentration cloud map

Fig.24 Three pipe spray structure distributed in the same plane with a vertical spacing of 300 mm, pipe length of 6451 mm, 5 g/m³ particle concentration test section velocity cloud map and particle concentration cloud map at the middle section of the test section under a wind speed of 100 m/s

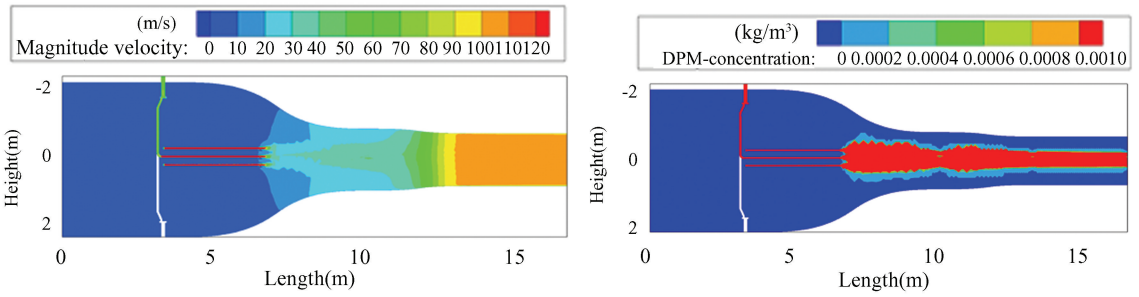

(a) Velocity cloud map (b) Particle concentration cloud map

Fig.25 Three pipe spray structure distributed in the same plane with a vertical spacing of 300 mm, pipe length of 3225 mm, and particle concentration test section with a 1 g/m³ particle concentration velocity cloud map and particle concentration cloud map at a wind speed of 100 m/s in the test section

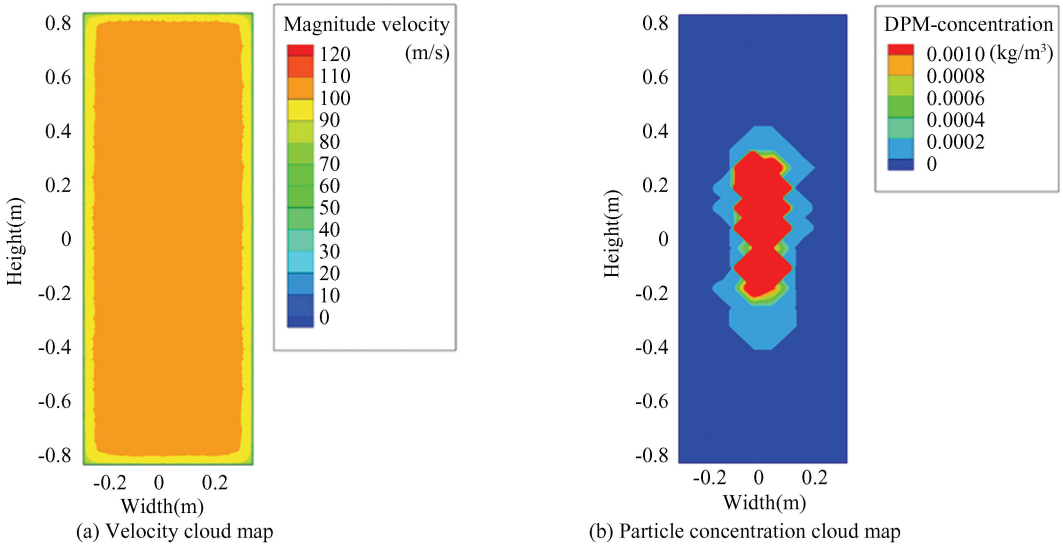

(a) Velocity cloud map (b) Particle concentration cloud map

Fig.26 Three pipe spray structure distributed in the same plane with a vertical spacing of 300 mm, pipe length of 3225 mm, 1 g/m³ particle concentration test section velocity cloud map and particle concentration cloud map at the middle section of the test section under a wind speed of 100 m/s

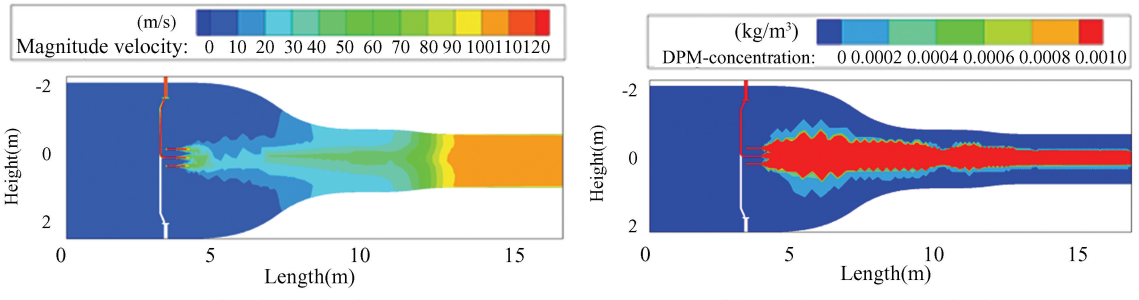

(a) Velocity cloud map (b) Particle concentration cloud map

Fig.27 Three pipe spray structure distributed in the same plane with a vertical spacing of 300 mm, pipeline length of 200 mm, 1 g/m³ particle concentration test section velocity cloud map and particle concentration cloud map at a wind speed of 100 m/s

In addition to studying the influence of different jet structures on the distribution of ice crystal particles, it is also necessary to investigate the effect of pipeline structure on airflow quality. In the paper, the stable inlet wind speed of 5.195 m/s is taken as the research condition, and 75% of the area in the middle section of the experimental section is extracted as the data extraction area to calculate the relevant airflow deviation angle and determine the degree of influence of different pipeline structures on airflow quality.

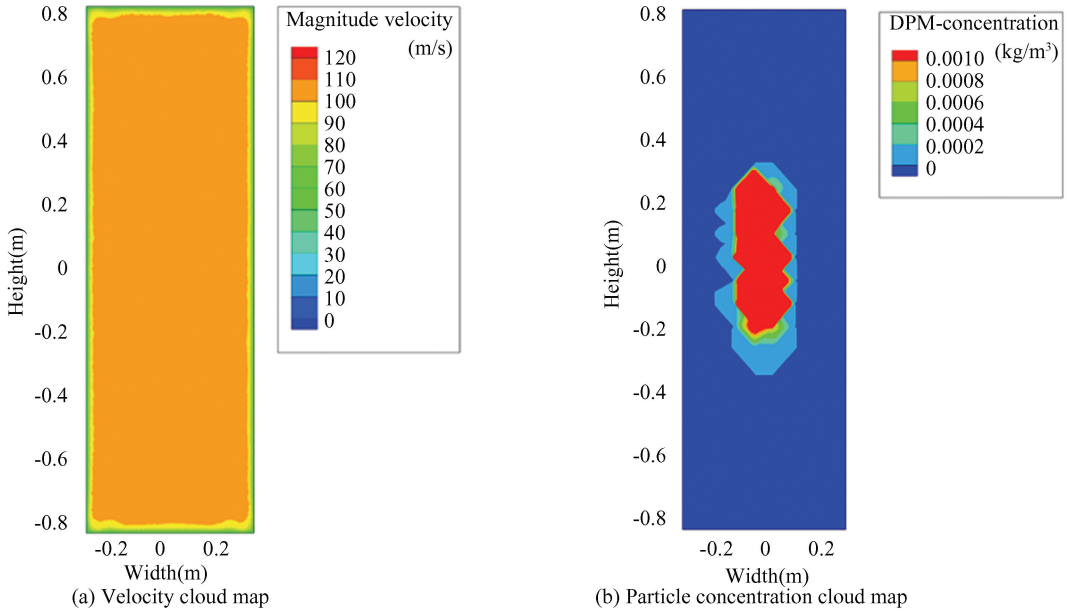

(a) Velocity cloud map (b) Particle concentration cloud map

Fig.28 Three pipe spray structure distributed in the same plane with a vertical spacing of 300 mm, pipe length of 200 mm, 1 g/m³ particle concentration test section velocity cloud map and particle concentration cloud map at the middle section of the test section under a wind speed of 100 m/s

The numerical simulation boundary conditions in this study include: The given pressure inlet conditions of supply system and nozzle inlet is 0.09 MPa; the wind speeds at the stable section entrance is 5.195 m/s, and the test wind speed is 100 m/s. The ice crystal particle flow rates in different structures are listed in Table 1.

The model used in this article is an unstructured grid, with a grid size ranging from 20 million to 40 million. The more complex the model structure, the greater the number of grids. The number and quality information of grids for all models are shown in Table 2.

Table 1 Ice crystal particle flow rates in different structures

Ice crystal particle flow rates (kg/s)	The desired concentration of ice crystal particles in the test section (g/m³)	Figures number
0.1	1	13,14,17,18,21,22,25,26,27,28
0.5	5	15,16,19,20,23,24

Table 2 Model information

Number of grids	Quality type criterion	Corresponding figures number
6248112	1.3×10^{-3}	13,14,15,16
26631160	6.8×10^{-6}	17,18,19,20
38710208	1.2×10^{-2}	21,22,23,24
30771982	1.8×10^{-3}	25,26
19619376	2.0×10^{-2}	27,28

The calculation formula for airflow deviation angle is as follows:

$$u_a^2 = u^2 + v^2 + w^2 \quad (15)$$

$$\tan\alpha = v/u_a \ ; \ \tan\beta = w/u_a \quad (16)$$

where u_a is airflow velocity; u, v, w are the velocity components of the airflow in the x, y, and z directions, respectively. α is the angle between the direction of airflow velocity and the y direction; β is the angle between the direction of airflow velocity and the z direction.

In Figs.29-33, numerical analysis was conducted on the influence of different types of pipeline jet structures on the air flow quality in the experimental section. From the figures, the airflow deviation angle $|\alpha|, |\beta| \leqslant 0.3°$ in the test section meets the requirements of relevant test standards, and different pipeline structures have little effect on the airflow deviation angle. As shown in Fig.29, it can be seen

from the velocity cloud map that the velocity uniformity deviation is less than 0.09%, when there is no pipeline structure present. As shown in Fig.30, the velocity uniformity deviation is less than 0.6%. As shown in Fig.31, the velocity uniformity deviation is less than 0.9%. As shown in Fig.32, the velocity uniformity deviation is less than 2.6%. As shown in Fig.33, the velocity uniformity deviation is less than 1.6%. In summary, the jet pipeline has a certain impact on the velocity uniformity distribution, while the impact on the airflow deviation angle is relatively small.

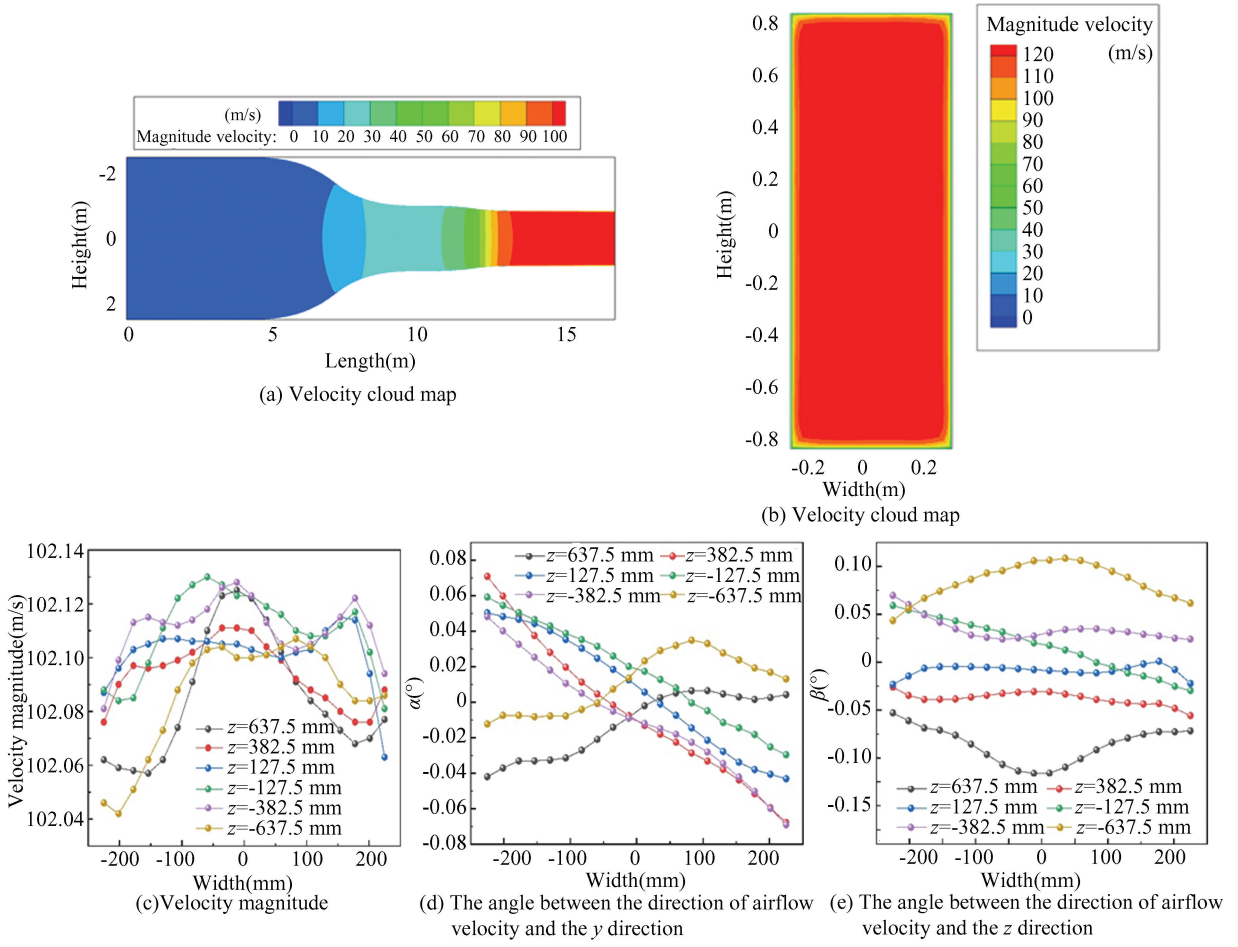

Fig.29 Distribution of velocity cloud map and calculation results of airflow deviation angle in the middle section of the wind tunnel test section without injection pipeline under the condition of inlet velocity of 5.195 m/s

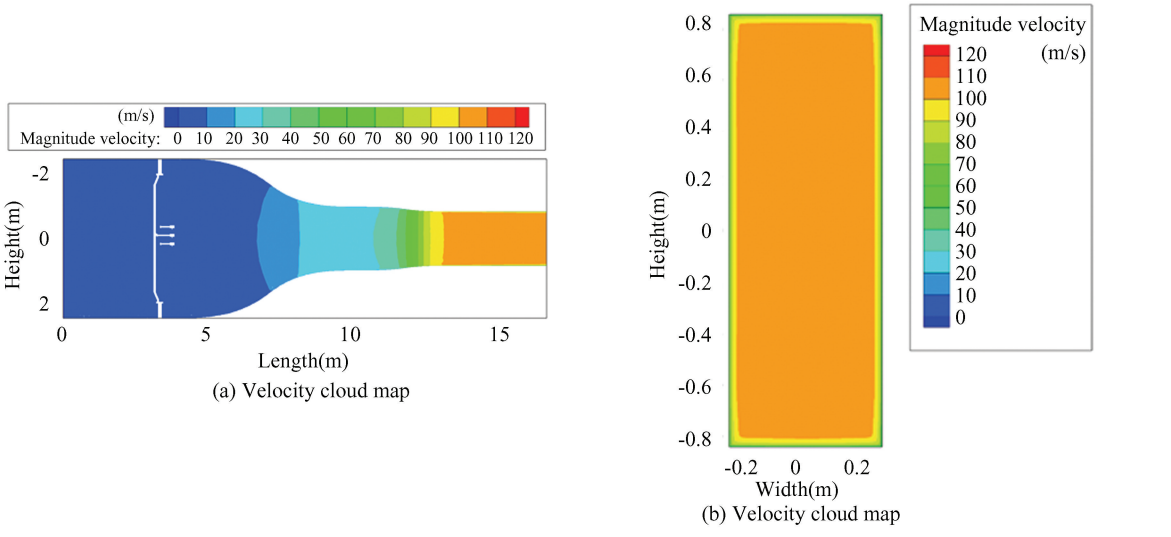

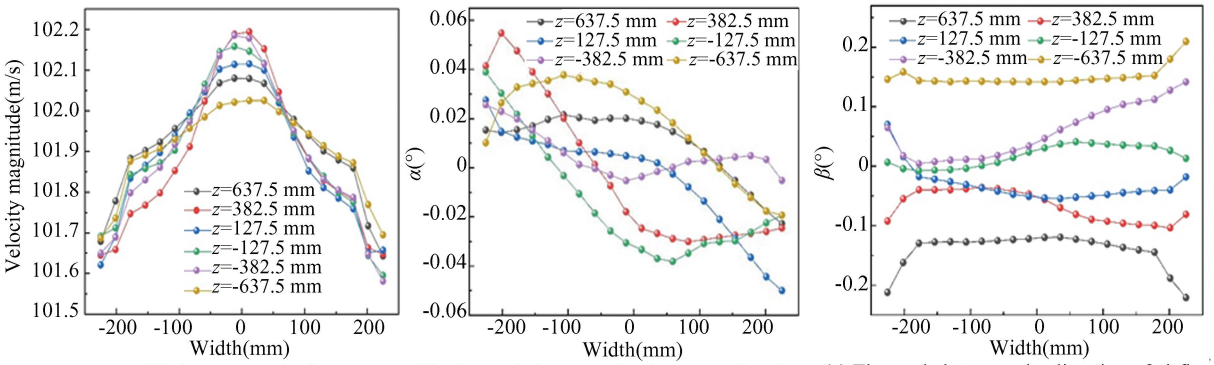

(c)Velocity magnitude (d) The angle between the direction of airflow velocity and the *y* direction (e) The angle between the direction of airflow velocity and the *z* direction

Fig.30 Under the condition of an inlet velocity of 5.195 m/s, a three-tube jet structure with a vertical spacing of 300 mm and a pipe length of 200 mm is distributed in the same plane. The velocity cloud map distribution and airflow deflection angle calculation results of the middle section of the wind tunnel test section are obtained

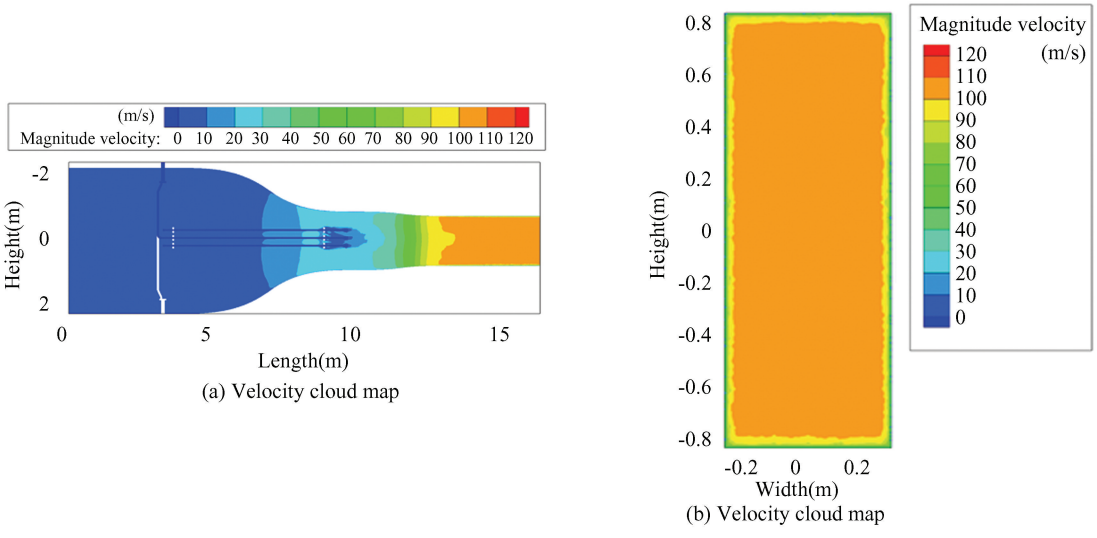

(a) Velocity cloud map (b) Velocity cloud map

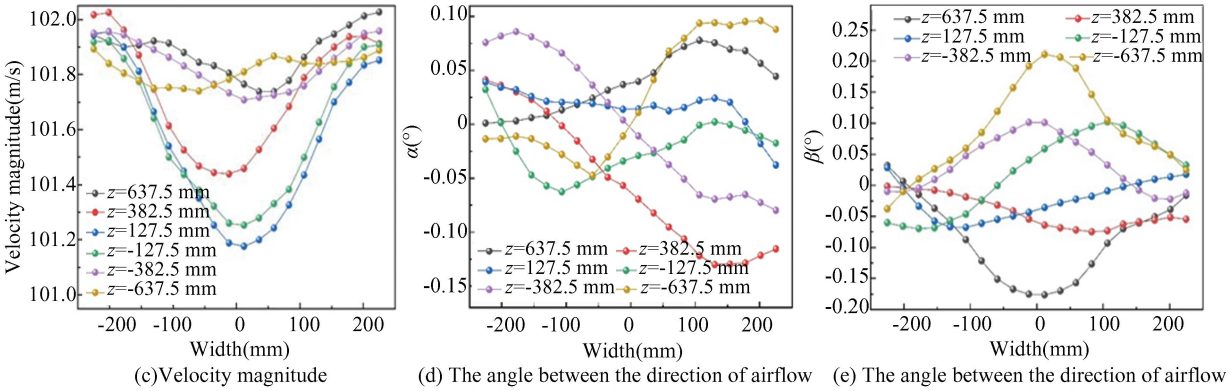

(c)Velocity magnitude (d) The angle between the direction of airflow velocity and the *y* direction (e) The angle between the direction of airflow velocity and the *z* direction

Fig.31 Under the condition of an inlet velocity of 5.195 m/s, a three-tube jet structure with a vertical spacing of 300 mm and a pipe length of 6451 mm is distributed in the same plane. The velocity cloud map distribution and airflow deflection angle calculation results of the middle section of the wind tunnel test section are obtained

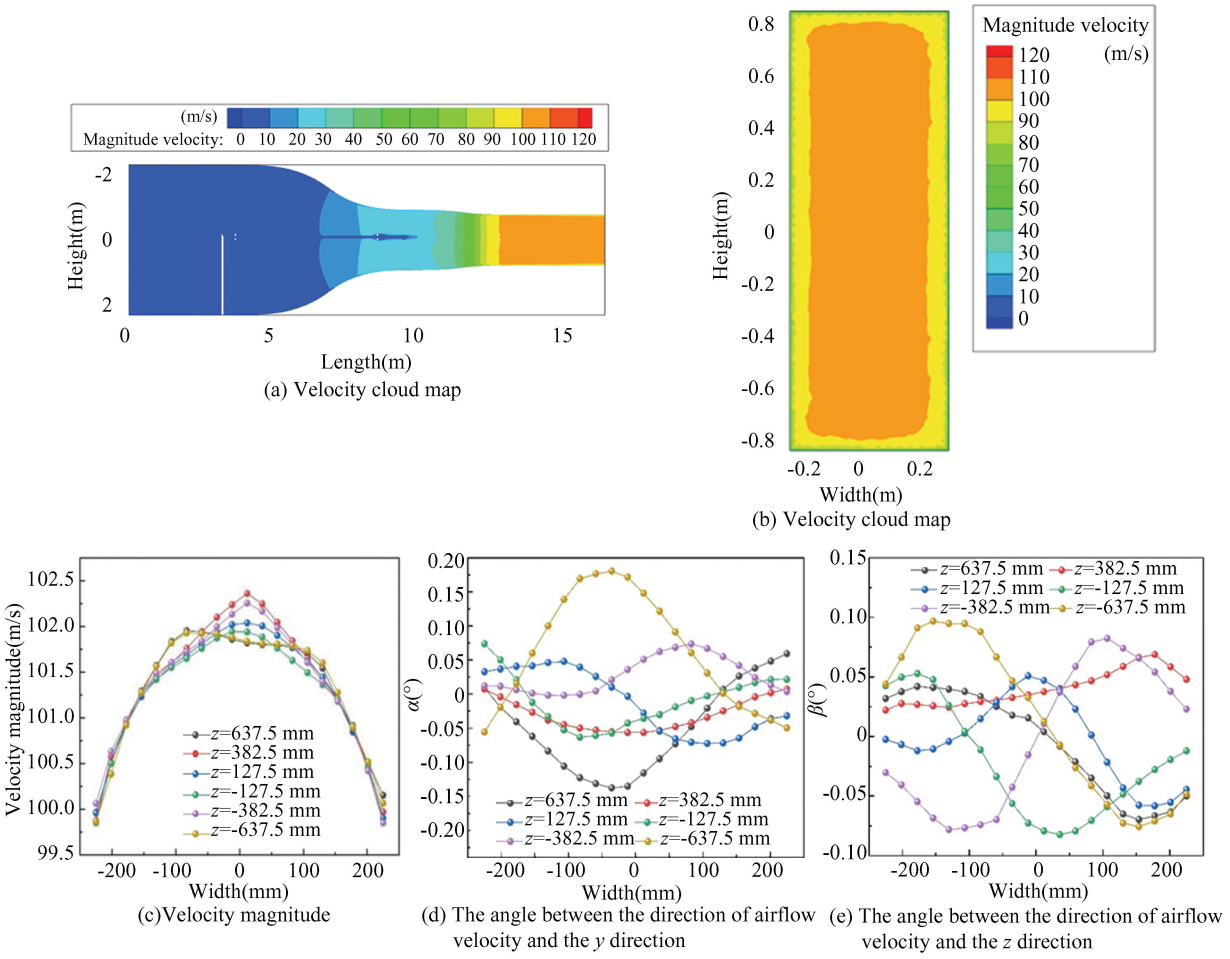

Fig.32 Under the condition of an inlet speed of 5.195 m/s, with a single tube structure and a pipeline length of 6451 mm, the distribution of velocity cloud map and calculation results of airflow deviation angle in the middle section of the wind tunnel test section

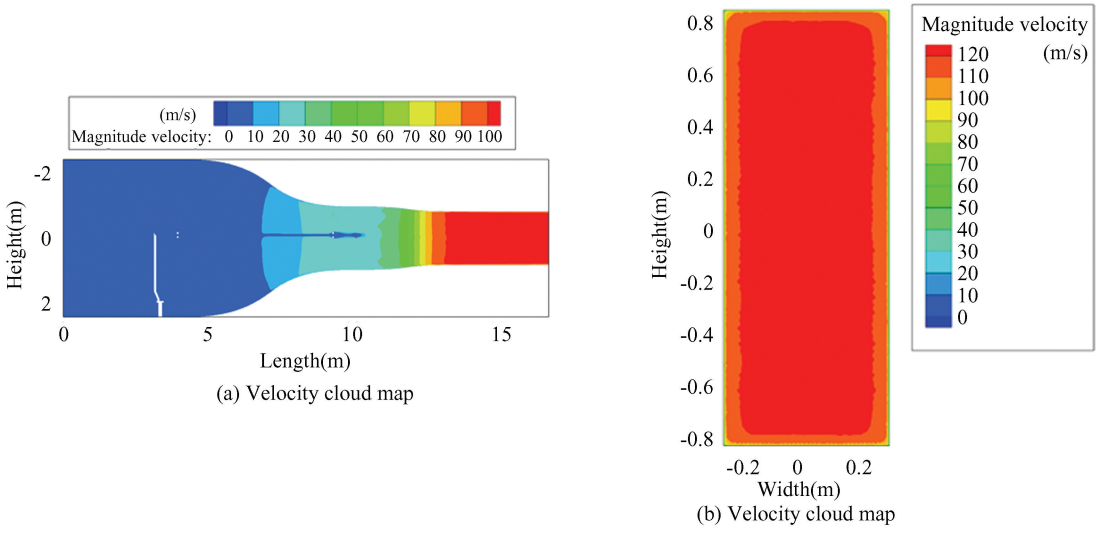

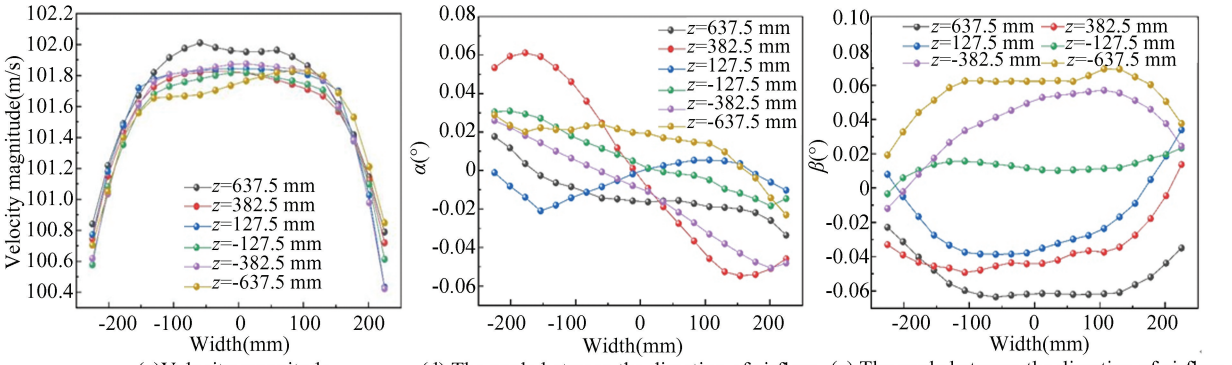

(c)Velocity magnitude (d) The angle between the direction of airflow velocity and the *y* direction (e) The angle between the direction of airflow velocity and the *z* direction

Fig.33 Under the inlet speed of 5.195 m/s, the three tube spray structure has a horizontal spacing of 120 mm, a vertical spacing of 600 mm, and a pipe length of 6451 mm, the velocity nephogram distribution and airflow deflection angle calculation results of the middle section of the wind tunnel test section

4 Conclusions

In this study, numerical simulations of the jet structure in the ice crystal multiphase flow test wind tunnel are conducted to evaluate the particle motion trajectory and concentration distribution of different jet structures, providing scheme support for the final selection of wind tunnel jet equipment. The numerical calculation of the impact of various jet pipe structures on airflow quality shows that the deviation angles of the airflow in both directions meet the relevant standard requirements, and the velocity uniformity is excellent. From the results on the concentration distribution of ice crystal particles, the shorter the length of the injection pipe, the larger the initial diffusion area of the particles, but eventually they will form a jet state. On the other hand, the spray pipes of the three-tube are on the same horizontal plane, and the shortest pipe length results in the best uniformity of ice crystal particles. Therefore, it can be selected as the optimal solution for the ice crystal particle spray structure.

References

[1] Su L W, Shen S C, Tian X P, et al. Research progress on ice crystal icing aeroengine. Aeroengine, 2023, 49(5): 89-99. (in Chinese)

[2] Shen H, Han B B, Zhang L F. Research progress of the ice crystal icing in aerp-engine. Journal of Experiments in Fluid Mechanics, 2020, 34(6): 1-7. (in Chinese)

[3] Lai Q R, Liu Q L, Guo L, et al. Icing and anti-icing test technology of aero-engine based on large-scale icing wind tunnel. Journal of Experiments in Fluid Mechanics, 2021, 35(3): 1-8. (in Chinese)

[4] Huang P, Bu X Q, Liu Y M, et al. Mixed phase/glaciated ice accretion: Review. Acta Aeronautica et Astronautica Sinica, 2022, 43(5): 025178 .(in Chinese)

[5] Yuan Q H, Fan J, Bai G C. Review of ice crystal icing in aero-engines. Journal of Propulsion Technology, 2018, 39(12):2641-2650.(in Chinese)

[6] Al-Khalil K, Salamon L, Tenison G. Development of the COX & Company icing research facility. Proceedings of the 36th AIAA Aerospace Sciences Meeting and Exhibit. Reston:AIAA, 1998:AIAA-1998-0097.DOI:10.2514/6.1998-97.

[7] Soeder R H, Andracchio C R. NASA Lewis Icing Research Tunnel User Manual. Washington, D. C. : NASA,1990,1: NASA TM-107159.

[8] Herman E. Goodrich icing wind tunnel overview, improvements and capabilities. Proceedings of the 44th AIAA Aerospace Sciences Meeting and Exhibit. Reston: AIAA,2006:AIAA-2006-862. DOI:10.2514/6.2006-862.

[9] Gent R W, Ford J M, Moser R J, et al. Results from super-cooled large droplet mass loss tests in the ACT Luton icing wind tunnel. Proceedings of the 41st AIAA Aerospace Sciences Meeting and Exhibit. Reston:AIAA,2003:AIAA-2003-389.DOI:10.2514/6.2003-389.

[10] Hammond D W, Luxford G. The Granfield university icing wind tunnel. Proceedings of the 41st AIAA Aerospace Sciences Meeting and Exhibit. Reston:AIAA, 2003:AIAA-2003-0901.DOI:10.2514/6.2003-901.

[11] Vecchione L, De Matteis P P, Leone G. An overview of the CIRA icing wind tunnel. Proceedings of the 41st AIAA Aerospace Sciences Meeting and Exhibit. Reston: AIAA, 2003:AIAA-2003-0900.DOI:10.2514/6.2003-900.

[12] Wendisch M, Garrett T J, Strapp J W. Wind tunnel tests of the airborne PVM-100A response to large droplets. Journal of Atmospheric and Oceanic Technology, 2002, 19(10): 1577-1584.DOI: 10.1175/1520-0426(2002)

019<1577:WTTOTA>2.0.CO;2.

[13] Guffond D P, Cassaing J J, Brunet L S. Overview of icing research at ONERA . Proceedings of the 23rd Aerospace Science Meeting. Reston: AIAA,1985: AIAA-1985-0335.DOI:10.2514/6.1985-335.

[14] Bartlett C S, Phares W J. Icing testing of a large full-scale inlet at the Arnold Engineering Development Center. Proceedings of the 23rd Aerospace Science Meeting. Reston: AIAA, 1993:AIAA-1993-0299.

[15] Flegel A B. Ice crystal icing research at NASA. Denver: Proceedings of the 9th AIAA Atmospheric and Space Environments Conference. Reston: AIAA, 2017: 20170006539.

[16] Flegel A B, Olver M J. Preliminary results from a heavily instrumented engine ice crystal icing test in a ground based altitude test facility. Proceedings of the 8th AIAA Atmospheric and Space Environments Conference. Reston:AIAA, 2016:AIAA 2016-3894. DOI:10.2514/6.2016-3894.

[17] Fuleki D M, MacLeod J D. Ice crystal accretion test rig development for a compressor transition duct. AIAA Atmospheric and Space Environments Conference. Reston:AIAA, 2010:AIAA 2010-7529.DOI:10.2514/6.2010-7529.

[18] Currie T C, Struk P M, Tsao J C, et al. Fundamental study of mixed-phase icing with application to ice crystal accretion in aircraft jet engines.4th AIAA Atmospheric and Space Environments Conference. Reston: AIAA, 2012: AIAA 2012-3035.DOI:https:10.2514/6.2012-3035.

[19] Crowe C T. Review-numerical models for dilute gas-particle flows . Journal of Fluids Engineering, 1982, 104(3): 297-303. DOI:10.1115/1.3241835.

[20] Sommerfeld M. Theoretical and experimental modeling of particulate flows, overview and fundamentals-Part I and II. von Karman Institute for Fluid Dynamics. Halle: Martin-Luther-Universität Halle-Wittenberg, 2000: 10 - 20.

[21] Crowe C T, Schwarzkopf J D, Sommerfeld M, et al. Multiphase Flows with Droplets and Particles. 2nd ed. Boca Raton: CRC Press, 2012.

[22] Cai Y L, Dong W. Calculation and analysis of heat and mass transfer for water droplet in icing tunnel test. Aeroengine, 2013, 39(3): 36-40. (in Chinese)

[23] Huang P, Bu X Q, Lin G P, et al. Phase transition characteristics of ice crystal particles in motion. Journal of Aerospace Power, 2022,37(7):1379-1391.(in Chinese)

[24] Zhang L F, Liu Z X, Zhang M H. Numerical simulation of ice accretion under mixed-phase conditions. Journal of Aerospace Engineering, 2016. 230 (13): 1 - 10. DOI: 10.1177/0954410015626734.